Solar Energy Materials & Solar Cells 248 (2022) 111985

Contents lists available at ScienceDirect

Solar Energy Materials and Solar Cells

journal homepage: www.elsevier.com/locate/solmat

Low temperature based PDINO cathode interlayer for high operational photostable inverted non-fullerene organic solar cells

Enas Moustafa [a], Maria Méndez [b], Josep Pallarès [a,**], Lluis F. Marsal [a,*]

[a] Department of Electric, Electronic and Automatic Engineering, Universitat Rovira i Virgili, Avda. Països Catalans 26, 43007, Tarragona, Spain
[b] Institute of Chemical Research of Catalonia-The Barcelona Institute of Science and Technology (ICIQ-BIST), Avda. Països Catalans, 16, 43007, Tarragona, Spain

ARTICLE INFO

Keywords:
PDINO cathode Interlayers
Non-fullerene organic solar cells
Photostability
Organic solar cells stability

ABSTRACT

The performance and industrial visibility of organic solar cells (OSCs) are greatly impacted by the functionality and stability of the interfacial layers. Many reported interface materials exhibited limitations in their fabrication temperature along with the operational stability toward the industrial up-scalability. In this work, a systematic analysis was conducted on the fresh and photo-aged-inverted non-fullerene organic solar cells (iNF-OSCs) with different structures of the electron transporting layers (ZnO, ZnO/PDINO, and PDINO), through studying their optical and electronic properties using external quantum efficiency measurements and impedance spectroscopy. Consequently, we presented PDINO as an efficient low temperature operation cathode interlayer for iNF-OSCs. Compared to the benchmark interface layers for i-OSCs such as ZnO, the PDINO interlayer used to replace the ZnO film, exhibiting a remarkable operational photostability. Where PDINO based iNF-OSCs demonstrated an extremely photostable behavior that is almost three times higher than the ZnO based devices under AM 1.5G (100 mW cm^{-2}) continuous illumination conditions. This behavior might be attributed to the PDINO interlayer properties, which undergoes with no photochemical reaction with the contacted PM6:Y7 photo-active layer, avoiding the inescapable photocatalytic effect that is commonly obtained by the ZnO interlayer.

1. Introduction

The power conversion efficiency (PCE) of organic solar cells (OSCs) has been promptly improved once emerging the recently developed non-fullerene small-molecules acceptors (NFAs), approaching PCE of 20% [1–6]. This remarkable increase in the power conversion efficiencies was due to the significant enhancement in the light absorption along with diminishing the energy losses [5,7–11], particularly upon minimizing the trade-off behavior between voltage loss and charge generation in nonfullerene organic solar cells (NF–OSCs) [12–14]. Despite the efficiency, long-term operational stability, particularly illumination stability, considers as a major challenging issue that must be confronted for the commercialization of OSCs [15–18]. Several strategies have been investigated to understand the intrinsic photo-degradation mechanism in order to overcome this recent demanding subject. Some of these avenues concern about the stability of the bulk-heterojunction photoactive blend microstructure through additives modifications to tune the properties of the photo-active layer [19–22]. Some other approaches determined the critical role of the interface materials stability and their compatibility with the contacted photo-active layer and electrodes, reflecting their importance for long-term stable OSCs [15,18,23–25]. This interface-induced instability approach is less frequently studied and still debatable even for high-performance systems. Moreover, the architecture of the OSCs has a pronounced impact on the stability of the devices as shown by M. T. Lloyd et al. group work [26], B. MacLeod [27] and several other reported studies, where the inverted structure assists the OSCs stability over the conventional structures from the scale of minutes up to years [25–31].

Furthermore, zinc oxide (ZnO) is the typically used cathode interlayer in inverted OSCs (i-OSCs), which exhibit better oxygen and humidity resistance as compared to the interface materials used in the conventional structure [25–29,32]. However, it possesses inescapable photo-instability behavior upon ultraviolet (UV) illumination, known as photocatalytic effect [33], resulting in photoinduced shunts and cause charge carrier recombination at the ZnO/photoactive layer interface, which in turn dramatically diminishing the performance of the corresponding devices [34]. Therefore, developing a compatible and photostable cathode inter layer materials that could provide efficient and

* Corresponding author.
** Corresponding author.
E-mail addresses: josep.pallares@urv.cat (J. Pallarès), Lluis.Marsal@urv.cat (L.F. Marsal).

https://doi.org/10.1016/j.solmat.2022.111985
Received 13 January 2022; Received in revised form 29 August 2022; Accepted 1 September 2022
Available online 13 September 2022

photostable OSCs classified as an urgent need for the scalability of OSCs. Thus, herein, we demonstrate the use of PDINO as a promising low temperature operation cathode interlayer that provides a highly photostable inverted non-fullerene organic solar cells (iNF-OSCs).

2. Experimental Methods

2.1. Materials

PM6(poly[2,6-(4,8-bis(5-(2-ethylhexyl-3-fluoro)thiophen-2-yl) benzo[1,2-b; 4,5 b']dithiophene))-alt-(5,5-(1′,3′-di-2-thienyl-5′,7′-bis (2-ethylhexyl)benzo[1′,2′-c:4′,5′-c']dithiophene-4,8-dione)]) polymer donor, Y7 (2,2'-((2Z,2′Z)-((12,13-bis(2-ethylhexyl)-3,9-diundecyl-12,13-dihydro- [1,2,5]thiadiazolo [3,4-e]thieno[2″,3'':4′,5']thieno [2′,3′,:4,5] pyrrolo[3,2-g]thieno[2′,3':4,5]thieno [3,2-b]indole-2,10-diyl)bis(methanylylidene))bis(5,6-dicholoro-3-oxo-2,3-dihydro-1H-indene-2,1-diylidene))dimalononitrile) nonfullerene acceptor and PDINO (*N*,*N*′-Bis(*N*,*N*-dimethylpropan-1-amine oxide)perylene-3,4,9,10-tetracarboxylic diimide) cathode interlayer were purchased from One-Material Inc. 1-chloronaphthalene (CN) solvent additive, 1-chlorobenzene solvent, ethanol, zinc acetate dehydrate and the hole transporting layer of vanadium oxide (V_2O_5) were supplied from Sigma-Aldrich. Finally, the metal contact with high purity silver (Ag) wire (99.99%) was purchased from Testbourne Ltd.

2.2. Device fabrication

The iNF-OSCs with structure of ITO/ETL/PM6:Y7/V_2O_5/Ag were constructed as follows. The indium tin oxide (ITO) pre-patterned glass substrate with the sheet resistance of 10 Ω cm^{-2} were ultrasonicated in detergent water, acetone, methanol, and isopropanol alcohol for 10 min, subsequently. The cleaned ITO-glass substrates were dried with nitrogen gun and transferred to an oven for 10 min at 100 °C. Before fabrication, the substrates were treated in ultraviolet-ozone for 15 min. The zinc oxide (ZnO) sol-gel precursor was prepared regarding our previous work [35–37]. 150 mg of zinc acetate dihydrate was dissolved in 1 mL of 2-methoxyethanol and 30 μL ethanolamine, then the mixture was left for 1 h under vigorous stirring at 70 °C, then after cooling it was diluted by methanol 1:1 (v/v) ratio to obtain ZnO precursor solution. The ZnO precursor solution was spin-coated on the top of the precleaned ITO substrates to deposit 30, and 30, 20 nm ZnO-film thicknesses for the A-ZnO-ETL and the optimization of B–ZnO/PDINO based devices, respectively, then annealed in air for 1 h at 200 °C. The ZnO-coated ITO substrates were transferred to a nitrogen-filled glove box for the PDINO and active layer deposition. Regarding the PDINO based devices, we prepared 1 mg/ml PDINO/methanol solution that stirred for 4 h. Then the PDINO solution was deposited over the ZnO film to obtain thicknesses of 10 and 15 nm for the optimization of B–ZnO/PDINO based devices, then 10, 20, and 35 nm for the optimization process of the C-PDINO based ones. It is important to note that all the device fabrication steps for devices C were conducted inside the glove box.

The PM6:Y7 blend was performed with the weight ratio of 1:1 dissolved in chlorobenzene to prepare the total concentration of 20 mg/mL solution. Then, the blend solution was stirred and heated at 80 °C for 3 h. 2 vol% of 1-chloronapthalene was added as solvent additives to the blend. The blend solution was spin-coated onto the A-ZnO, B–ZnO/PDINO and C-PDINO substrates to obtain an active layer thickness around 100 nm. Then, the prepared films were treated with 100 °C for 1 h. The substrates were finally transferred into an evaporation chamber inside the glove box where 5 nm of V_2O_5 and 100 nm Ag were sequentially deposited under high vacuum conditions ($\leq 1 \times 10^{-6}$ mbar). The V_2O_5 layer was deposited at a rate of 0.05 kÅ/s and the Ag film rate was 0.1 kÅ/s for the initial 10 nm thickness then increased to 0.4 Å/s till 100 nm film thickness that performed in 190 min [38] with effective devices area of 0.09 cm^2. Finally, we transferred the fabricated devices from the evaporator to the sample holder inside the glove box which was carefully sealed for the device's measurement steps.

2.3. Device measurement and characterization

The thicknesses of the prepared films within the devices were measured by the surface profilometer (AMBIOSTECHNOLOGY-XP 1). The current density – voltage (J-V) characteristics were extracted using a Keithley 2400 Source Measure Unit with a solar simulator (Abet Technologies model 11000 class type A, Xenon arc) as an artificial light source. The standard light intensity of the AM 1.5G spectrum was calibrated by an NREL certified monocrystalline silicon photodiode. The devices were tested under illumination at the standard light intensity of 100 mW cm^{-2}. Moreover, dark measurements were performed to obtained J-V dark curves. Furthermore, all the J-V characteristics were performed at room temperature in the forward direction from −1 to 1 V, with a scan step of 0.01 V. V_{OC} and J_{SC} over different light intensity were obtained by *J-V* measurements under the solar simulator using a set of optical density filters. The external quantum efficiency (EQE) measurements were conducted via Lasing IPCE-DC model under a forward wavelength sweep direction from 300 nm to 1100 nm. The photoluminescence (PL) measurement carried out on a Fluorolog Horiba Jobin Yvon spectrofluorimeter using 600 nm excitation wavelength. Impedance spectroscopy (IS) measurements were performed under simulated AM 1.5G illumination using an HP-4192A impedance analyzer. Impedance data were extracted at three different DC levels: J_{SC} point, near V_{mpp}, and close to V_{OC}. The IS experimental data were fitted using Ivium software analyzer. The performance of the devices was tested both prior to and after the impedance measurements with no significant sign of degradation. All measurements were conducted under N_2 atmosphere where all devices were measured in a sealed holder that was carefully closed inside the glove box under an N_2 atmosphere (the holder photo presented in the SI Fig. S1). Blend films morphologies topography images were obtained by atomic force microscopy (AFM) in a tapping mode using silicon probes with a spring constant of 1–5 N m^{-1} and a resonant frequency of 75 kHz. Molecular Imaging Pico SPM II instrument (pico+) software was used to analyze the surface morphology images. Finally, the transmittance spectra were conducted using PerkinElmer Lambda 950-UV/vis/NIR spectrometer with an integrating sphere at room temperature.

3. Results and discussions

In this work, we fabricated the iNF-OSCs using three different structures of electron interfacial layers. Where, bilayer stack of PDINO/ZnO (named Type B-based devices) and PDINO (named Type C- based devices) were used as cathode interlayers to fabricate iNF-OSCs with the configuration of ITO/ETL/PM6:Y7/V_2O_5/Ag as illustrated in Fig. 1a. Moreover, control devices with ZnO as cathode electron transporting layer (ETLs) that optimized in our previous work [37] were used for comparison (named Type A-based devices). The schematic energy levels of the fabricated iNF-OSCs were demonstrated in Fig. 1b. The performance of the fabricated iNF-OSCs to optimize the interlayers in Type B and C devices incorporating different thickness of ZnO and PDINO films was displayed in Figs. S2a and b using the representative current density-voltage (J-V) characteristics under simulated AM 1.5G illumination at 100 mW cm^{-2}. In addition, the photovoltaic performance parameters statistics were summarized in Table S1. Accordingly, we selected devices-III of type B (III–B) with ZnO/PDINO bilayers thicknesses of 20/10 nm, respectively and devices II of type C (II–C) with PDINO film thickness of 20 nm as the optimized devices that illustrated in the PCE % box plots in Figs. S2c and d and Table S1. Furthermore, the fabrication parameters and procedures were described in the 2.2. Device Fabrication in the 2. Experimental Methods section.

The control ZnO-based devices (A-ZnO-ETL) in our previous report [37] exhibited a maximum power conversion efficiency (PCE_{Max}) of 13.62% with an average open-circuit voltage (V_{OC}) of 0.75 V, a short

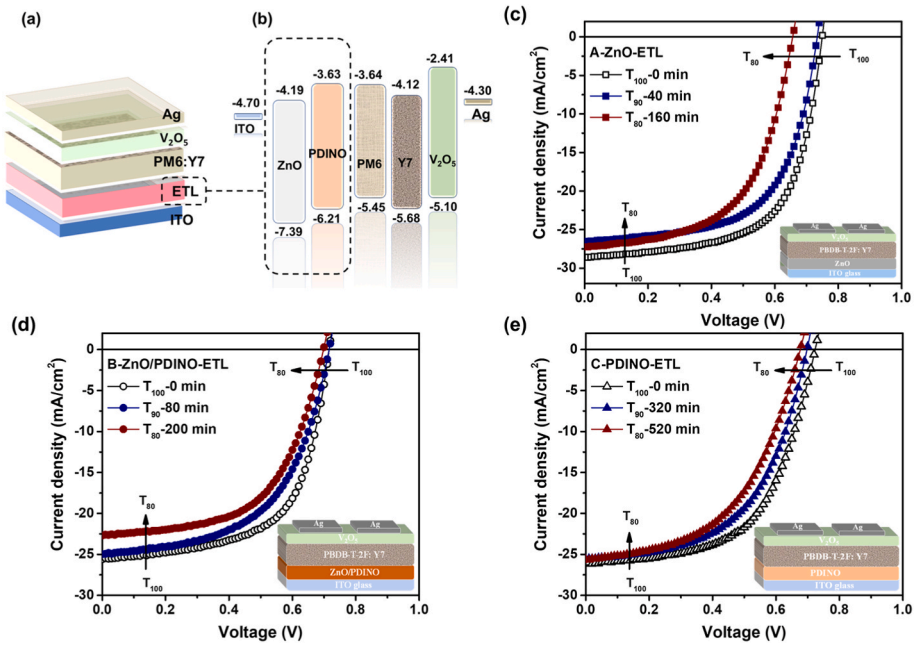

Fig. 1. (a) Schematic diagram of the fabricated iNF-OSCs structure, (b) the energy band diagrams of the inverted OSCs, current density-voltage (J–V) characteristic curves under AM 1.5 G illumination of the photo-aged (c) A-ZnO (d) B–ZnO/PDINO and (e) C-PDINO based devices.

circuit current density (J_{SC}) of 28.61 mA cm^{-2}, fill factor (FF) of 0.64, series (R_S) and shunt (R_{Sh}) resistances of 1.20 and 382 Ω cm^2, respectively. Using the optimized ZnO/PDINO stacking bilayer cathode (B–ZnO/PDINO-ETL) based devices, we obtained a reduction of the PCE_{Max} to 11.40% and the J_{SC} to 25.77 mA cm^{-2} as well as a slight diminishing in the average V_{OC} (0.72 V), FF (0.61) and R_{Sh} (344 Ω cm^2) along with a bit increase in the R_S average values to 1.65 Ω cm^2. Same behavior was observed for the PDINO-based devices (C-PDINO-ETL) that revealed a PCE_{Max}, average V_{OC}, J_{SC}, FF, and R_S of 10.91%, 0.72 V, 26.15 mA cm^{-2}, 0.58 and 4.71 Ω cm^2, respectively. In contrast, the R_{Sh} values where slightly improved to 397 Ω cm^2 as listed in Table 1.

The previously mentioned devices of types A (A-ZnO), B (B–ZnO/PDINO) and C (C-PDINO) were determined to perform the photostability aging test under continues exposure of simulated AM 1.5G illumination condition (100 mW cm^{-2}) as demonstrated in Fig. S1, following the international Summit on OSC Stability ISOS Standard [39] till achieving 80% of their initial PCE-T_{100} values (T_{80}). The T_{100} is the time of the initial PCE values of the fresh-prepared devices, T_{90} is the time reaching 90% of their initial PCE as explained by the protocol [39]. During the Photo-aging test measurements, the devices were kept under continues light exposure and measured every 10 min for the first 20 min, then every 20 min till the 80 min, then every 40 min till the T_{80} degradation time as presented in the inset labels of Fig. S3. In this study, we pointed out the significant effect obtained by the photo-aging test. Therefore, it was conducted in an inert atmosphere of <0.1 ppm O_2 < 0.1 ppm H_2O using the sealed samples holder mentioned previously, to avoid the possible degradations that might arise from the oxygen and the ambient moisture.

Fig. 1c,d,e depicts the T_{100}, T_{90} and T_{80} J-V characteristics of the A-ZnO, B–ZnO/PDINO and C-PDINO based devices under continues illumination. In addition, the devices T_{90} and T_{80} lifetimes are summarized in Table 2, as well the decrease in the performance of the photo-aged devices over time was described in Fig. S3. Moreover, the normalized PCE values are summarized in Fig. 2a. It was surprising to obtain that the lowest T_{100} performance devices possessed by the PDINO interlayer (C-PDINO) exhibited excellent photostability, maintaining 80% of their efficiency after 520 min illumination, while the B–ZnO/PDINO based devices showed a lower photostability by reaching their T_{80} after 200 min. However, the highest T_{100} performance ZnO-based control iNF-OSCs demonstrated a rapid decay in the PCE presenting an accelerated degradation, achieving T_{80} after 160 min only under same condition, which agreed with the recent work reported by M. Cui et al. [15]. Hence, it is worthy to notice that after achieving T_{80}, the C-PDINO based devices

Table 1
Inverted organic solar cells performance parameters statistics of the T_{100} fresh, T_{90} and T_{80} photo-degraded devices over photo-aging times under AM 1.5 G illumination.

Device Type	V_{OC} (V)	J_{SC} (mA/cm^2)	FF	PCE (%)	PCE_{MAX} * (%)	R_S (Ω cm^2)	R_{Sh} (Ω cm^2)
A-ZnO-ETL							
T_{100}- 0 min [37]	0.75 ± 0.02	28.61 ± 0.33	0.64 ± 0.09	13.04 ± 0.58	13.62	1.20 ± 0.13	382 ± 61
T_{90}- 40 min	0.73 ± 0.01	26.12 ± 0.82	0.61 ± 0.03	11.46 ± 0.42	11.88	1.31 ± 0.24	362 ± 26
T_{80}- 160 min	0.66 ± 0.01	27.01 ± 0.62	0.52 ± 0.04	10.11 ± 0.41	10.52	2.41 ± 0.14	314 ± 12
B–ZnO/PDINO-ETL							
T_{100}- 0 min	0.72 ± 0.01	25.77 ± 0.21	0.61 ± 0.02	11.00 ± 0.40	11.40	1.65 ± 0.14	344 ± 22
T_{90}- 80 min	0.72 ± 0.01	25.01 ± 61	0.55 ± 0.06	9.81 ± 0.08	9.89	2.15 ± 0.21	289 ± 24
T_{80}- 200 min	0.70 ± 0.01	22.69 ± 0.47	0.57 ± 0.04	9.00 ± 0.03	9.03	2.05 ± 0.11	342 ± 46
C-PDINO-ETL							
T_{100}-0 min	0.72 ± 0.01	26.15 ± 0.23	0.58 ± 0.04	10.26 ± 0.65	10.91	4.71 ± 0.23	397 ± 51
T_{90}- 320 min	0.70 ± 0.02	25.80 ± 0.42	0.54 ± 0.03	9.55 ± 0.20	9.75	3.64 ± 0.61	364 ± 46
T_{80}- 520 min	0.68 ± 0.02	25.62 ± 0.63	0.51 ± 0.02	8.63 ± 0.21	8.84	4.88 ± 0.19	238 ± 61

The statistics average values of the performance parameters based on 9 devices.

Table 2
Photostability lifetime of the photo-aged iNF-OSCs under AM 1.5G illumination.

Standard lifetime	A-ZnO-ETL	B–ZnO/PDINO-ETL	C-PDINO-ETL
T_{90} (min)	40	80	320
T_{80}(min)	160	200	520

showed almost 3 times longer lifetime than the ZnO-based devices (control-A-ZnO and B–ZnO/PDINO) under same photo-aging conditions as simplified in Table 2. Furthermore, it is important to note that in early minutes, the ZnO based devices (Type A and B) demonstrated a faster decay than the C-PDINO based devices that clarified in Fig. S4. This phenomenon is known as a "burn in loss" degradation behavior which is commonly observed performance loss under light [20,40]. This intrinsic light-driven degradation is believed to be due to the material properties [19,41,42] and the photochemical reaction between the interfacial layers and the photoactive layer [18,40,43,44]. Hence, we can observe that the C-PDINO based devices exhibited insignificant burn in loss effect that reflecting their outstanding photostable behavior.

Moreover, we can clearly see a sharp burn in loss of the V_{OC} and FF values regarding the control A-ZnO based devices as shown in Fig. 2b and c, V_{OC} reached 88% while the FF achieved 82% after only 160 min of illumination. This detected attitude might reveal the fast photo-degradation behavior observed for Type A devices. Unlike the stabilized V_{OC} and FF for the C-PDINO based devices, V_{OC} showed a consistence slow decrease and maintained 95% (Fig. 2b) and the FF remained 88% (Fig. 2c) after prolonged 520 min illumination, providing a remarkable photostability behavior. It is worth to mention that the V_{OC} losses commonly obtained due to the light-induced trap states/defects which reveal the traps in the devices as reported by N. Gasparini et al. work [45]. Upon this context, we can depict that the C-PDINO based devices possessed lower photo–induced defects within the devices than the ZnO based ones (Type A and B). This might attributed to replacing the ZnO layer with the PDINO film that avoids the inescapable photocatalytic behavior of the ZnO that would facilitate the decomposition of the organic active blend result in photo-instability issues upon the UV illumination as exhibited elsewhere [15,33,42,46].

Interestingly, the overall J_{SC} values were diminished for both A-ZnO-ETL and B–ZnO/PDINO based devices (Fig. 1c and d, Fig. 2d) over photo-aged time, in contrast to the C-PDINO based devices that almost maintained its J_{SC} values till 520 min (T_{80}-almost 9 h) (Figs. 1e and 2d). However, it was interesting to observe a 2% increase in respect of the J_{SC} initial values after 90 min of illumination for the A-ZnO based cells, then a sharp decrease till the T_{80} after 160 min. This increment in the J_{SC} values may deliver from the UV-irradiation dependence, reported as light-soaking effect [47,48]. This light-soaking phenomenon was widely observed for the inverted OSCs using ZnO or other metal oxide materials as ETL as well as it is highly considered to evaluate the photostability behavior of the photo-aged OSCs [49–51]. There are two main suggested mechanisms behind the origin of this phenomenon. First, it may obtain from the photo-induced rearrangement of the Fermi levels at the ITO/metal oxides interfaces upon the filling of trap states during the illumination, that diminishes the potential barrier and thus enhance the electron extraction through the ITO/metal oxide interface [47,50,52,53]. Second, the interfacial dipole clue role between the metal-oxide/organic blend film interface as reported elsewhere [52,54,55]. Interestingly, this observed effect for the A-ZnO based devices was highly matched with the previously discussed PCE, V_{OC} and FF burn in loss behavior that verifies the rapid photo-degradation of these devices. Accordingly, we think that the different T_{80} lifetimes between the fabricated devices systems are due to the intrinsic photostability variation of the ZnO and PDINO ETLs. Moreover, it was pronounced that the insertion of the PDINO layer between the active blend and the ZnO film in the B–ZnO/PDINO based devices acts as a shield that partially suppresses the accelerated photo-degradation arise from the ZnO photocatalytic effect appeared in the A-ZnO based devices. Therefore, by avoiding the ZnO in the C-PDINO based devices, they did not manifest any light soaking behavior reflecting the good quality of the devices [52] along with obtaining very week effect of burn in loss providing stunning photostability behavior.

For further investigation regarding the obtained performance parameters of the photo-aged fabricated i-OSCs, we performed the J-V characteristic for the T_{100} fresh, the T_{90} and T_{80} i-OSCs at dark as shown in Fig. 3a,b,c. As displayed in Fig. 3a, the A-ZnO based devices suffered from an almost two orders in magnitude increased leakage current under the reverse bias condition as compared to the fresh devices after 2.5 h continuous illumination. Such behavior indicates a high shunt possibility recognized as "photo-induced shunts" that responsible for

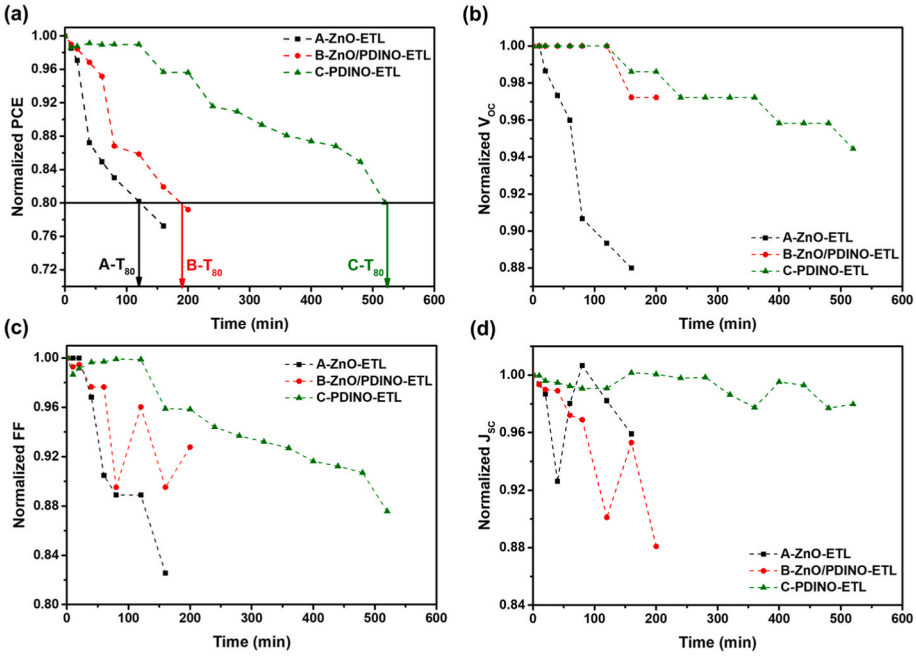

Fig. 2. Normalized performance parameters of the iNF-OSCs (a) PCE, (b) V_{OC}, (c) FF, and (d) J_{SC} of the iNF-OSCs over photo-aging time.

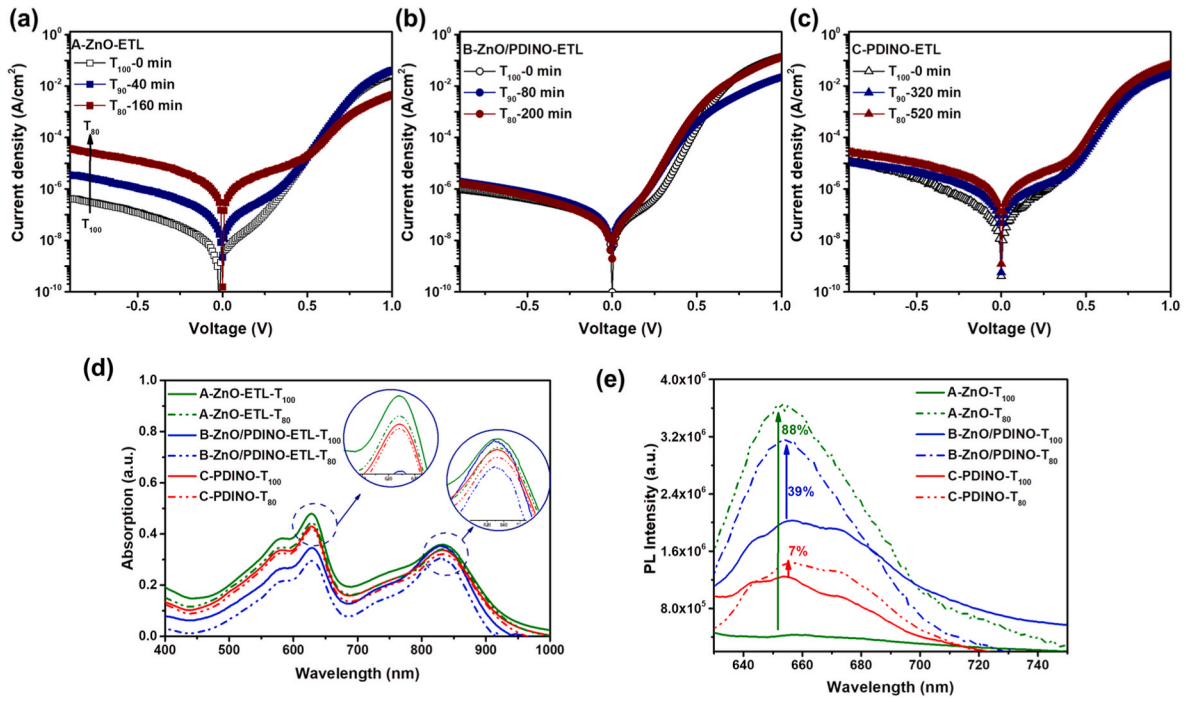

Fig. 3. J-V characteristic curves of the T_{100} fresh and T_{90}, T_{80} photo-degraded iNF-OSCs at dark of (a) A-ZnO, (b) B–ZnO/PDINO, and (c) C-PDINO based devices, (d) UV–vis optical characteristics of the T_{100} and T_{80} photo-aged PM6:Y7 blend films over different ETLs, (e) Photoluminescence spectra of the T_{100} and T_{80} photo-aged PM6:Y7 blend films over different ETLs.

diminishing the charge carrier at the semiconductor/ZnO selective interface [56], which is responsible for lowering the J_{SC} in the device, in addition, low R_{Sh} is in charge of the low FF in the OSCs [57]. This obtained result agreed with the fast performance decay upon the illumination as demonstrated in Fig. 2a and Table 1. In clear contrast, B–ZnO/PDINO and C-PDINO based devices (Fig. 3b and c) revealed more stable behavior even after longer time of photo-degradation. This underlining the remarkable photostability of the PDINO based devices especially the C-PDINO ones that showed inconsiderable change even after almost 9 h of constant illumination.

Furthermore, Fig. 3d demonstrates the UV–visible absorption spectra for the PM6:Y7 blend over the ITO/ZnO (A-ZnO-ETL), ITO/ZnO/PDINO (B–ZnO/PDINO-ETL) and ITO/PDINO (C-PDINO-ETL) samples before (T_{100}) and after (T_{80}-as Listed in Table 2) the AM 1.5G illumination to evaluate the absorption spectra under same photo-aging conditions. After the illumination, we can see that the ZnO-based films (Type A and B) illustrate a significant diminishing in the peaks intensity (inset photo), reflecting the interface and blend decomposition via the photocatalytic activity of the ZnO, which in agreement with the work by M. Cui and co-workers [15]. In contrary, the C-PDINO based films showed more sustained absorption spectra even after prolonged 520 min of illumination.

As further evidence that the remarkable reduced photocatalytic activity of the PDINO is responsible for the lifetime enhancement, we investigated the previously mentioned T_{100} and T_{80} aged films through photoluminescence (PL) spectroscopy as presented in Fig. 3e. The photo-degraded ZnO based films showed a dramatically increased PL intensity of 88% for A-ZnO based films. This implies a crucial inhibition of the exciton dissociation for the respective photo-aged devices, which is considered one of the key reasons for the rapid initial photo-degradation [16,17,58]. Same behavior was observed by L. Duan et al. using different fullerene and non-fullerene active blend, indicating that the presence of ZnO assists the decomposition of the contacted blend layer upon illumination due to the previously discussed photocatalytic effect of the ZnO [16]. Unlike the C-PDINO based films, where the PL spectrum increased only 7% compared to the fresh films upon 520 min under light. This indicated that the excitons maintain their efficient dissociation ability into charge carriers [16,17,58] even after longer time of exposure announcing the champion photostability behavior of C-PDINO based films.

Finally, it was interesting to find that the B–ZnO/PDINO based film showed an increment of the PL intensity by 39% after 200 min which is right between the A-ZnO and the C-PDINO based films, providing a clear proof that the presence of PDINO reduced the photocatalytic activity along with improving the lifetime of the fabricated devices. Herein, this observation is highly consistent with the obtained performance results for the corresponding devices from the J-V characterization.

The charge recombination mechanisms within the devices regarding the photo-aging test were further explored through investigating the light intensity (P_{Light}, from 0.1 to 100 mW cm^{-2}) dependence of the T_{100}-fresh and T_{80}-photodegraded i-OSCs J-V characteristics. The J_{SC} and V_{OC} as a function of P_{Light} were plotted in logarithmic scale along with the linear fitting as presented in Fig. 4a,b,c and 4d,e,f, respectively. The relation between the J_{SC} and P_{Light} was modeled as $J_{SC} \propto P_{Light}^{S1}$, where S_1 represents the power law exponent. Under short circuit condition, S_1 value should approach 1 if the bimolecular recombination is insignificant, and values less than 1 implies that the bimolecular recombination of the free charge carriers will limit the photocurrent of devices [59,60].

In Fig. 4a,b,c, we observed a difference in the dependency behavior at low and high light intensities. At low P_{Light} (<1 mw/cm^2), the linearly fitted S_1 values for all devices were quite similar as well as at T_{100} and T_{80} conditions (around 0.62–0.64 which is less than 1) that pronounces a major effect of bimolecular recombination. But different attitude was observed for the S_1 values at high P_{Light} (>10 mW cm^{-2}), where the S_1 values for the T_{100} fresh A-ZnO, B–ZnO/PDINO and C-PDINO devices were 0.99, 0.96, and 0.91, respectively. Despite, these observed values depicted that the A-ZnO based iNF-OSCs exhibited the lowest bimolecular recombination which greatly matched with its highest initial performance (Table 1). But S_1 values for the entire T_{100} devices are close to unity. Hence, it is worth to note that, regarding the T_{100} fresh prepared devices, the diminishing in the J_{SC} of structure B and C based devices as compared to A ones, might be due to the transmittance behavior of the

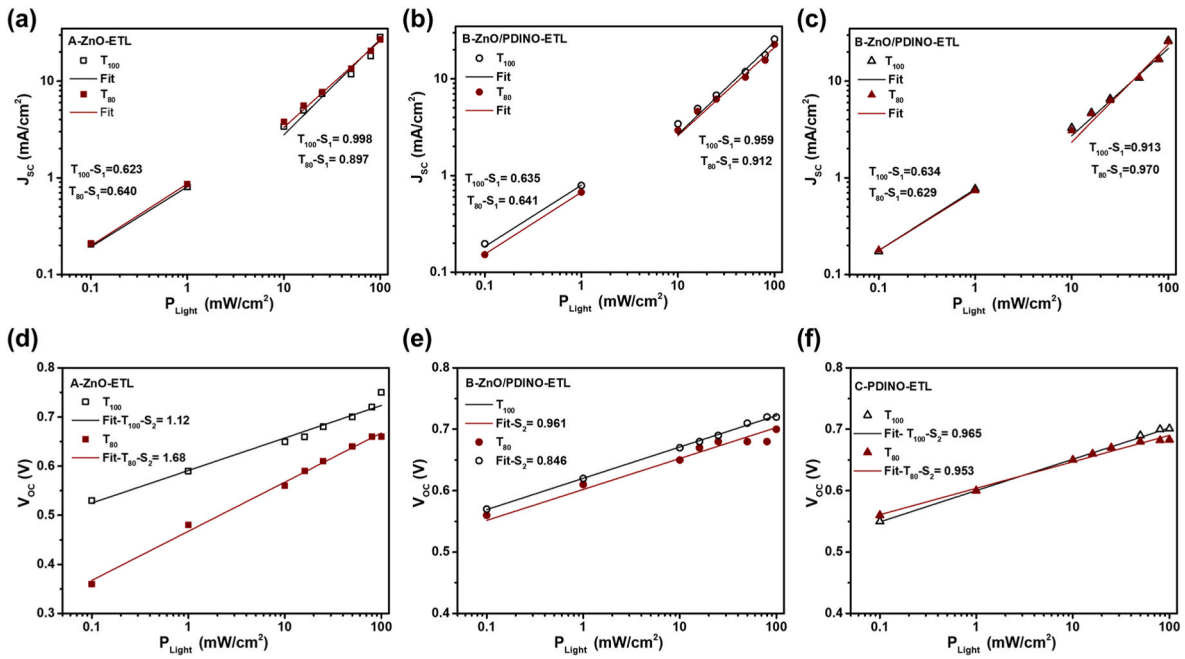

Fig. 4. T_{100} and T_{80} iNF-OSCs (a,b,c) J_{SC} and (d,e,f) V_{OC} versus the light intensity (P_{light}), symbols for the experimental data and the line for the fitted data.

ETLs as presented in Fig. S5 not because of the recombination behavior. Where B–ZnO/PDINO and C-PDINO based films showed the lower film transmittance, indicating lower amount of light could reach the photo-active blend and in turn lower value of generated current (Table 1). However, after the T_{80} photo-aged of the device (listed in Table 2), we exhibited that the S_1 values were 0.89, 0.91, and 0.97, respectively, reflecting more implemented bimolecular recombination within the A-ZnO based devices upon the illumination (for 2.5 h only) than the others. This behavior explains the rapid photo-degradation behavior that observed for Type A devices as previously discussed (Fig. 1d).

Interestingly, C-PDINO based devices showed a pioneer behavior in photo-degradation resistance with smaller extent of bimolecular recombination presenting almost same S_1 value after prolonged illumination time of 520 min. This attitude verifies the stable J_{SC} values over the illumination aging time test and in turn the highest photostability of this kind of devices. Hence, it can be notice that the order of the T_{80}-S_1 values of the corresponding iNF-OSCs is consistent with their obtained photostability behavior (Fig. 2a).

To gain more insights into the recombination kinetics inside the fresh and photo-degraded devices, we display their semi-logarithmic V_{OC} dependence vs P_{Light} (Fig. 4d,e,f) that followed the Shockley diode equation [61–63] of:

$$V_{OC}\alpha S_2\left(\frac{KT}{q}\right)Ln(P_{light})\alpha n_{id}\left(\frac{KT}{q}\right)Ln(J_{SC}) \quad (1)$$

where, n_{id} is the ideality factor of the diode ($n_{id} = S_2/S_1$), k is the Boltzmann constant, T is the temperature, and q is the elementary charge. S_2 values (Fig. 4d,e,f insets) were calculated by fitting Equation (1), then obtaining the n_{id} values of 1.12, 1.01 and 1.06 for the T_{100} fresh A-ZnO, B–ZnO/PDINO and C-PDINO i-OSCs, respectively. It is apparent that all fresh devices has almost similar n_{id} values, indicating that the bimolecular recombination is governing the charge recombination in the fresh iNF-OSC devices along with insignificant trap-assisted recombination process [64–66]. After the illumination of T_{80} times of the examined devices, the n_{id} value for the A-ZnO was clearly escalated to 1.87 (Fig. 4d), underlining the dominated trap-assisted recombination mechanism upon 2.5 h of the samples photo-aging due to the increase of trap density [67,68]. In contrary, we surprisingly found that the n_{id} values of the both T_{80} photo-aged B–ZnO/PDINO and C-PDINO based devices were 1.00 and 1.01(Fig. 4e and f), implying a negligible trap-assisted recombination behavior within the devices, resulting in most stable V_{OC} values over aging time. We suggest that, in case of the PDINO based devices, the interfacial trap-assisted recombination was effectively diminished upon the photo-induced light which enhance the photostability of the devices. These observations are coherent with the observed photostability behavior of the photo-aged devices (Figs. 1 and 2). It explains the rapid decay of the V_{OC}, FF and in turn the PCE over the AM 1.5G aging time upon the light-induced trap formation in the A-ZnO based devices. In addition, it clarifies the remarkable photo-stability behavior of the entire performance parameters in the photo-aged C-PDINO based i-OSCs (Figs. 1 and 2 and Table 1).

To further understand the charge dynamics behind the dramatic decrease of the performance of the ZnO based device as well as the perceptible photostability of the C-PDINO based cells upon the photo-aging test, we measured the photocurrent density (J_{Ph}) vs the effective voltage (V_{eff}) of the fresh and photo-aged devices in double logarithmic scale as plotted in Fig. 5a,b,c. J_{Ph} equals J_L-J_D, where $J_L$and J_D are the photocurrent densities under illumination and dark current densities, respectively. V_{eff} is defined as V_O–V, where V_O is the voltage when $J_L = J_D$ and V is the applied bias voltage [64,69,70]. This dependence of the J_{Ph} on the V_{eff} assists the calculation of the exciton dissociation probabilities (P_{diss}), maximum amount of absorbed photons that provides the dissociation and generation of free carriers (G_{max}) and the generation rate (G_{rat}) of the free charge carriers in the fabricated devices [71,72] as listed in Table S2 of the T_{100}-fresh and the photo-aged (T_{90} and T_{80}) samples (calculation details explained in the SI). For the entire tested samples, we found that the J_{Ph} increased linearly at low V_{eff} (<0.3 V), then it starts to saturate by increasing the V_{eff} > 0.3 V, representing an efficient photogenerated charge carrier that can extracted by the electrodes [71,73]. Regarding the P_{diss} of the fresh devices, A-ZnO, B–ZnO/PDINO and C-PDINO based devices were calculated as 98.44, 98.10, and 98.58%, respectively, then after exposure to light till T_{80} they obtained values of 96.57% (within 160 min), 96.94 (within 200 min) and 96.32% (within 520 min), respectively. For fair comparison, it worthy to notice, despite all the devices presented almost same value of P_{diss} over the photo-aging time, but C-PDINO based devices showed the longest time to achieve this value, which is closely related to the high photostability of the devices, in contrast to the other ZnO based cells.

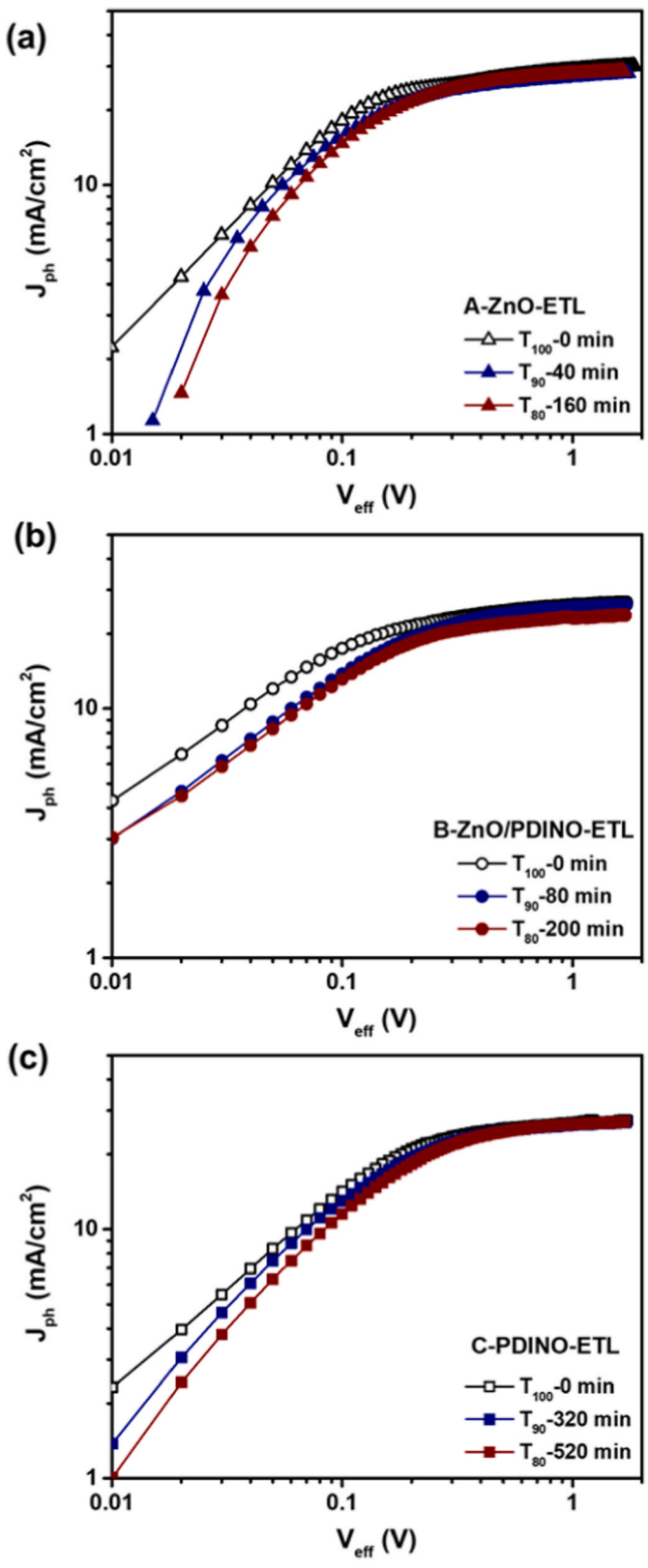

Fig. 5. J_{Ph} versus V_{eff} characteristics of the T_{100}, T_{90} and T_{80} (a) A-ZnO, (b) B–ZnO/PDINO, and (c) C-PDINO based devices over photo-aging time.

This results was in good matching with the stabilized performance parameters over photo-aging time for the C-PDINO based devices (Figs. 1 and 2), as well as it correlated with the lowest T_{80} recombination behaviors discussed in Fig. 4 c,f.

Furthermore, the G_{max} and the G_{rat} for the fresh devices were following the same trend of their performances (Table 1), where A-ZnO > B–ZnO/PDINO > C-PDINO as listed in Table S2. However, by approaching the T_{90} and T_{80} of the samples photo-aging test, we disclosed that the G_{max} and the G_{rat} were decreased for types A and B samples but it showed a fascinating sustained behavior even with longer photo-aged time than the others (Table S2).

By combining the obtained results from the light intensity dependence on J_{SC} and V_{OC}, along with the voltage dependence of J_{Ph}, a side from the PCE values, C-PDINO based devices revealed week recombination losses in addition to highest resistance time toward the photo-aging test, which accounting their superior improvement of its operational photostability.

As a part of investigating the mechanism behind the photo-degradation within the fabricated i-OSCs, external quantum efficiency (EQE) measurements were conducted for the fresh and the photo-aged devices. It is worth to mention that all measurements were performed under same condition of 1 sun, AM 1.5G illumination to evaluate a proper comparison with the other characteristics.

Fig. 6a,b,c depict the plots of EQE versus the photon energy for A-ZnO, B–ZnO/PDINO and C-PDINO based devices, respectively. it can be seen that the photocurrent spectrum response of the entire devices is up to 1.4 eV [74] regarding same photo-active blend of PM6:Y7. Hence, the higher photocurrent response of the devices is more probably correlated to the excitation of the active polymer blend, and the lower photocurrent response than 1.4 eV is more likely attributed to the charge transfer states [75,76]. Accordingly, the Urbach energy (E_U) of the devices was defined with the absorption tail (known as Urbach tail) below 1.4 eV by following Equation [74,77].

$$\alpha(E) = \alpha_0 \, e^{(E-E_g)/E_U} \tag{2}$$

where, E represent the photon energy, α (E) is the light absorption coefficient, α_0 is the optical absorption coefficient at the band edge, and E_U is the estimated Urbach energy. The E_U value reveals the trap-mediated charge recombination [78] which represents the energetic disorder in the molecular orbitals [75,77]. The extracted E_U values of the fresh and photo-aged i-OSCs were presented in the corresponding insets in Fig. 4a, b,c. We manifested that both photo-aged types of A and B ZnO-based devices showed a noticeable increase in the T_{90} and T_{80} E_U values as compared to the T_{100}-fresh corresponding devices. A higher E_U usually indicates a higher energetic disorder that originates the reduction of the device performance via implemented density of state distributions that assist the recombination [78], which determined as a common reason for fast initial photo-degradation of the photo-aged devices. This observation gives a proper declaration regarding the V_{OC} and FF burn in losses [79] along with the produced trap-assisted recombination that leads to the rapid photo-degradation behavior exhibited by the ZnO-based devices, particularly A-ZnO ones, as presented in the previously discussed characteristics. However, by avoiding the presence of the ZnO in the C-PDINO based devices, we obtained the most stable E_U values over the photo-aging test time (inset of Fig. 6c). This withstand attitude pointed out the insignificant existence of trap-mediated charge recombination and in turn less displayed energetic disorder upon 520 min of illumination.

Fig. 6c,d,e illustrate the EQE response of the fresh and photo-degraded samples over wavelength rang of 300–1100 nm. Regarding A-ZnO based devices, the photo-aged devices showed a noticed diminishing in the absorption over the full range (Fig. 6c), which suggested to be related to the insufficient charge extraction and transport mechanism, which greatly matched with the performance drop obtained for the photo-aged A-ZnO cells with in 160 min, discussed in the J-V characteristics (Figs. 1 and 2). Moreover, in case of the photo-aged B–ZnO/PDINO based cells, we can observe that at T_{80}, the absorption reduction did not carry out over the full wavelength range (such A-ZnO cell), but it started from 500 nm then sharply decreased (Fig. 6d). This

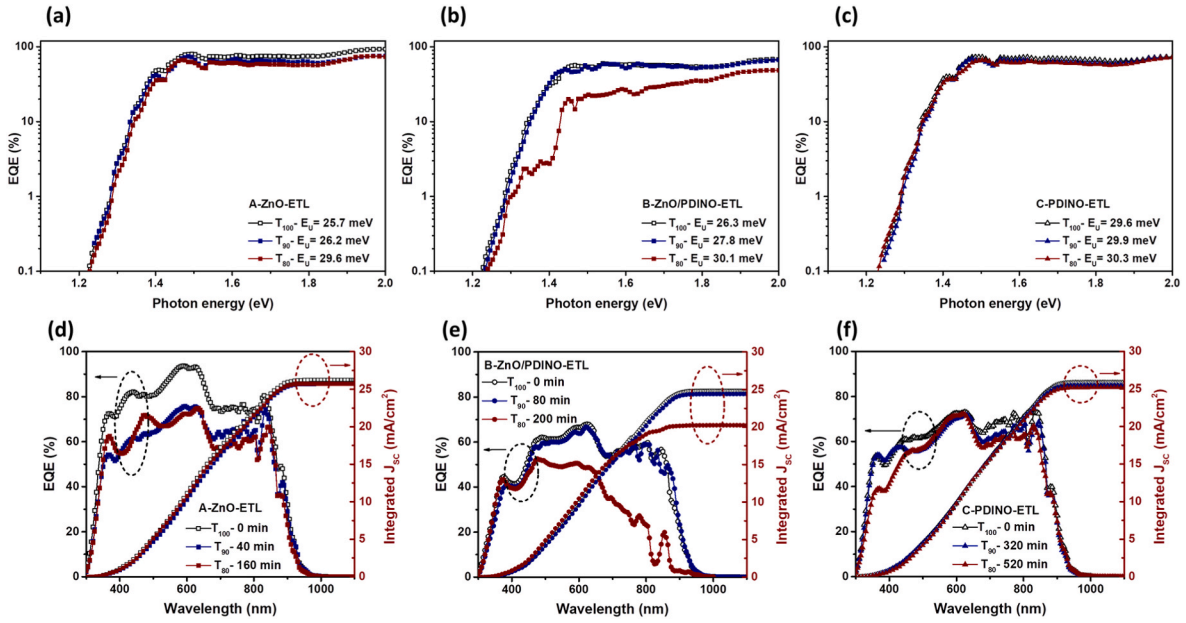

Fig. 6. EQE vs photon energy of the (a) A-ZnO (b) B–ZnO/PDINO, (c) C-PDINO iNF-OPVs with the inset values of Urbach energy (E_U), EQE spectra (left) and the integrated short circuit current (right) of T_{100}, T_{90} and T_{80} photo-aged (d) A-ZnO (e) B–ZnO/PDINO, (f) C-PDINO iNF-OSCs.

obtained behavior might reflects that despite the presence of the PDINO layer between the ZnO and active blend may partially assist the device resistance toward photo-degradation and extended the cells lifetime to 200 min, but the ZnO still has the pronounced photocatalytic contribution of degrading the contacted layers and as a sequence assists the decay of the device performance. Furthermore, the exhibited EQE reduction for both types of A and B photo-aged devices is consistent with the observed J_{SC} loss from the J-V characteristics (Fig. 2d). While the photo-aged C-PDINO based devices signify inconsiderable decrease of the EQE absorption response, indicating the most photo-stable behavior over aging test time (for 520 min) as compared to the fresh ones (Fig. 6f). This obtained behavior is perfectly coherent with the stabilized J_{SC} values obtained over photo-aging time by the J-V characteristics in Fig. 2d. Furthermore, the calculated integrated J_{SC} values from the EQE spectra for the fresh T_{90}, and T_{80} photo-aged devices were listed in Table S2, which consistent with the values obtained from the J-V measurements under AM 1.5G illumination with the maximum error values less than 10% (Table 1).

Impedance spectroscopy was carried out under AM 1.5G illumination condition as an alternative insight study to investigate the electronic properties of the fabricated devices with respect to the interfacial charge transfer and carrier recombination [80] along with providing the mechanisms behind the performance deterioration of the photo-aged tested devices. Hence, we conducted the capacitance-frequency (C*f*) measurements to calculate the trap density of state (DOS) that explained in the supplementary information in Equation S1,S2. Fig. 7 displays the evaluated trap-DOS curve as a function of energy for the fresh and the T_{80} photo-degraded devices. It demonstrates a single exponential trap distribution which defines the same trap activation energy and carrier response within the devices [81,82]. Furthermore, after the T_{80} photo-aging time (Table 2), a decline in the DOS values for a given frequency can be revealed for all devices. This behavior can be explained as DOS energy shift of E_O (explained by Equation S3 in the supplementary information). Thus, the T_{80} photo-aged devices demonstrated lower energy, reflecting higher interfacial induced defects in the devices compared to the T_{100} fresh ones as an intrinsic origin of tarps [35, 83–86].

In consequence, we measured the values of the energy shifting (X) for the T_{80} photo-degraded cells, which explained in the supplementary information, presented by the blue line in Fig. 7. We detected that the order of energy sifting value (X) is following the trend of A-ZnO > B–ZnO/PDINO > C-PDINO. Hence, C-PDINO based cells provided lower shifting value of X than the ZnO-based ones, indicating less trapped sites implemented in these cells, confirming their superior photostable behavior toward the illumination. Interestingly, A-ZnO based devices showed the highest X value of double, demonstrating highest contribution of photo-induced traps within the device. Moreover, we can clearly notice that the T_{80} ZnO-based devices (A and B types) possessed an additional impeded deep-trap sites [82,87] (Fig. 7a and b), that did not observe for the T_{80} C-PDINO based i-OSCs (Fig. 7c), consisting with their rapid photo-degradation performance, particularly the drop in the FF and V_{OC} [79,88], presented by the J-V and EQE characteristics. It is worth to mention that this sequence of attitude is highly matched with the obtained sequence behavior of the previously discussed E_U values over photo-aging times in Fig. 6a,b,c, depicting same observation of energy disorder upon trap creation.

Furthermore, impedance Nyquist test was performed to gain a better understating of the photo-degradation effect within the tested devices. The obtained data from the IS was originated from the response testing of the devices under AM 1.5G illumination and an applied AC signal with 5 mV amplitude in the frequency range between 5 Hz and 2 MHz. Fig. 8 shows typical Nyquist plots that were obtained for the T_{100} fresh and T_{80} photo-aged iNF-OSC and their corresponding Bode plots presented in Fig. S6 [42] at V_{OC}. All plots exhibited a semicircle shape, reflecting the efficient transfer at the active layer/electrode interface [80]. As an initial observation, we can notice that all the devices obtained a single process represented by one arc behavior. In addition, the diameter of the arc increased for the photo-aged devices over aging times (Table 2), considering the increment in the bulk resistance of the devices upon the continuous light exposure [89]. Nevertheless, it was interesting to notice that this increment is much higher in the A-ZnO based devices, unlike C-PDINO based ones. Same behavior was observed for photo-aged devices at maximum power point voltage (V_{mpp}) and short circuit current (Voltage = 0 V) in Fig. S7. Accordingly, it is worth to mention that the size of the arc is commonly correlated to the device resistance [80]. Hence, to gain more information about the physical parameters of each layer within the fresh and photo-aged cells, we analyzed the plots with an electrical equivalent circuit using Debye model [37,90]shown in Fig. S8, which provided a proper fitting for the experimental data (presented as solid lines in Fig. 8). The equivalent circuit contains, R_S

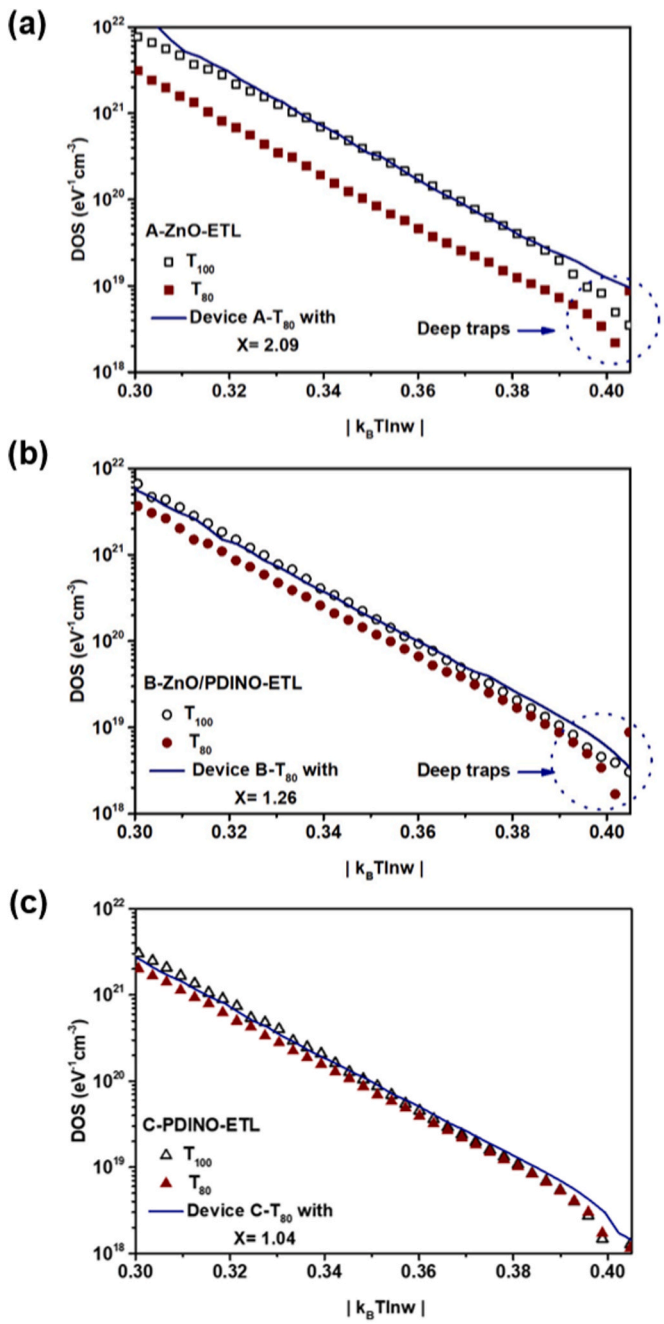

Fig. 7. DOS as function of $|k_BTln\omega|$ at V_{OC} under AM 1.5G illumination of the T_{100} and T_{80} photo-aged iNF-OPVs over times (blue line with shifting value of X), (a) A-ZnO, (b) B–ZnO/PDINO, and (c) C-PDINO based devices. (For interpretation of the references to colour in this figure legend, the reader is referred to the Web version of this article.)

represents the series resistance which indicates the resistance of the contact and the ohmic components [35,80]. A parallel association of resistor (R) and capacitor (C) for 3 RC elements in series, where R represents the resistance of electrons transportation in each layer as R_1, R_2 and R_3 refers to ETL, PM6:Y7 and the V_2O_5 layer, respectively. In addition, C refers to the geometrical dielectric component capacitance values of each layer. Moreover, the R_4C_4 were in series which attached in parallel to R_2C_2 corresponding the photo-active layer (PM6:Y7) obeying Debye model [90], explaining the effect of the photo-degradation behavior that carried out in the photo-active blend within the A, B and C based devices regarding the variation of the contacted ETLs. This model considers the existence of a single type of trap implemented in one layer [90] upon the continuous illumination process. Finally, L is the included inductor applied to fit the data properly at high frequency [80]. Then, the extracted parameters from the fitting were listed in Table S4.

The exhibited fitting capacitance values for each layer were highly matched with the theoretical values shown in Table S5. This might imply that at V_{OC}, the IS data was controlled by the geometrical capacitances provided by the metal insulator-metal model indicating the presence of fully depleted layers [91].

Regarding the fitted resistance values for each layer of the T_{100} fresh and T_{80} photo-aged devices (Table S4), it can be seen that the R_S values were at the range of 3.0–5.0 Ω in the entire devices. This might indicate that the different ETLs did not show a significant effect in the ITO/ETL interface upon the photo-aging test. Similar behavior was observed for the V_2O_5 layers, which show consistent resistance values (R_3) before and after the phot-aging test for the entire devices as presented in Table S4 and Fig. S9.

On one hand, as for the T_{100} and T_{80} A-ZnO based devices, we found that the R_1 values of the ZnO layer slightly increased for from 28 to 33 Ω, respectively. While the R_2 values were almost doubled from 20 to 43 Ω (Fig. S9a). In turn, the total resistance (R_{total}) of the device were increased from 67 to 79 Ω (Table S4), which controlled by the photo-active blend resistance (R_2). This obtained behavior is greatly matched with the escalated R_S values obtained by the J-V measurements under illumination over aging times (Table 1). Moreover, it confirms the burn in losses effect observed for the A-ZnO performance parameters, especially the V_{OC} and FF parameters, which leads to their rapid photo degradation behavior (Figs. 1 and 2).

On the other hand, regarding the B–ZnO/PDINO based devices, the R_1-ZnO values were 22 and 28 Ω for the T_{100} and T_{80} photo-aging time, respectively, while R_1-PDINO values were 8 and 11 Ω, respectively. In addition, the R_2 values were 64 Ω for the T_{100} devices and 66 Ω for the photo-aged devices (Fig. S9b). From the obtained fitted values, we can notice that both R_1 and R_2 values showed a slight increment in their resistance values after the photo-aging test (200 min), where the R_{Total} values rather increased from 79 to 92 Ω (Table S4). This attitude confirms their higher photo-stability as compared to the A-ZnO ones (Fig. 2a). Furthermore, T_{80} C-PDINO based cells showed the highest stable R1 and R2 values (Fig. S9c) with respect to the longest exposure time to the light (520 min) as compared to the T_{100} fresh ones. Where, the R_1, R_2 and R_{Total} presented a bit increase from 25 to 30 Ω, from 64 to 66 Ω and from 106 to 117 Ω, respectively. This explains the steady R_S values obtained by the J-V measurements (Table 1) over aging time which in turn provided a superior J_{SC} photo-stability behavior (Fig. 2d). Accordingly, to perform a fair comparison regarding the fitted resistance values between the T_{100} and T_{80} of each device, we considered the thickness difference of each device and then calculated the variation of R_{Total}/thickness percentage as illustrated in Fig. 8d. We found that A-ZnO based devices exhibited the highest ratio of resistance increment by 22.2%, while the B–ZnO/PDINO cells increased by 9.6% and the C-PDINO based ones increased by only 8.8%. This obtained results explains the much higher variation in the arc diameters that obtained for the A-ZnO-devices (Fig. 8a) and the less variation exhibited for the C-PDINO based devices (Fig. 8d). With respect to the T_{80} times (Table 2), it was considered the lowest for A-ZnO devices, reveling their fast photo-degradation behavior, and the highest for the C-PDINO cells, marking their impressive photostable behavior.

Finally, it is worth to mention that the key reason of the highest resistance variation obtained by the A-ZnO based devices might be attributed to photocatalytic effect of the ZnO film, which highly accelerated the photo-degradation the photo-active blend (Fig. S9a) and in turn the entire devices [33]. Interestingly, the resistance variation was diminished by adding the PDINO layer between the ZnO and the photo-active blend as observed in the B–ZnO/PDINO devices. As well, this difference in the resistance values was highly suppressed by replacing the ZnO with PDINO, which avoid the photo-degradation of

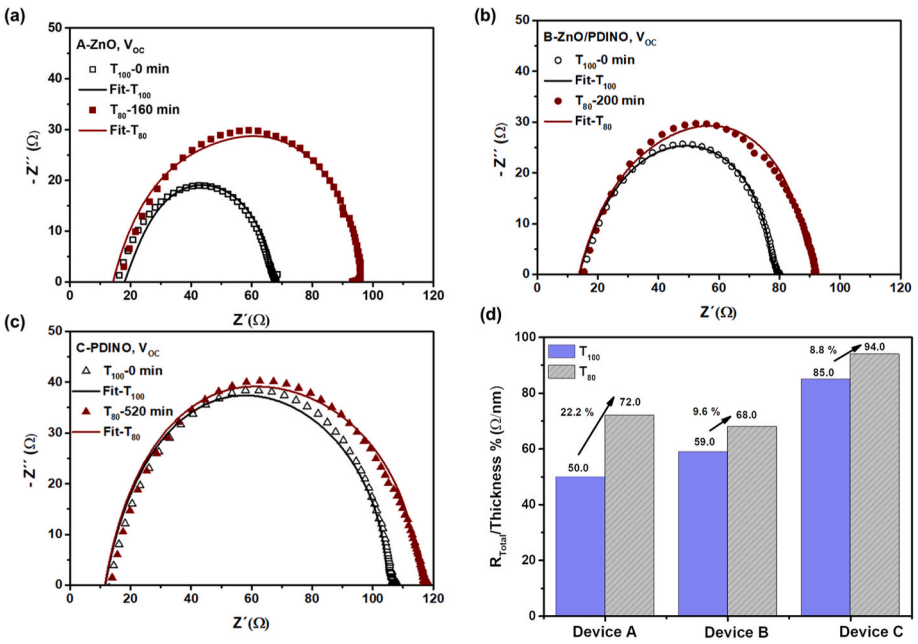

Fig. 8. Nyquist plots at V_{OC} under AM 1.5G illumination of the T_{100} and T_{80} photo-aged (a) A-ZnO, (b) B–ZnO/PDINO, and (c) C-PDINO based devices, using symbols for the experimental data and the fitting results in solid lines by applying the equivalent circuit in Figs. S8 and (d) the total resistance variation of the T_{100} and T_{80} iNF-OSCs with respect to the total thickness within each device.

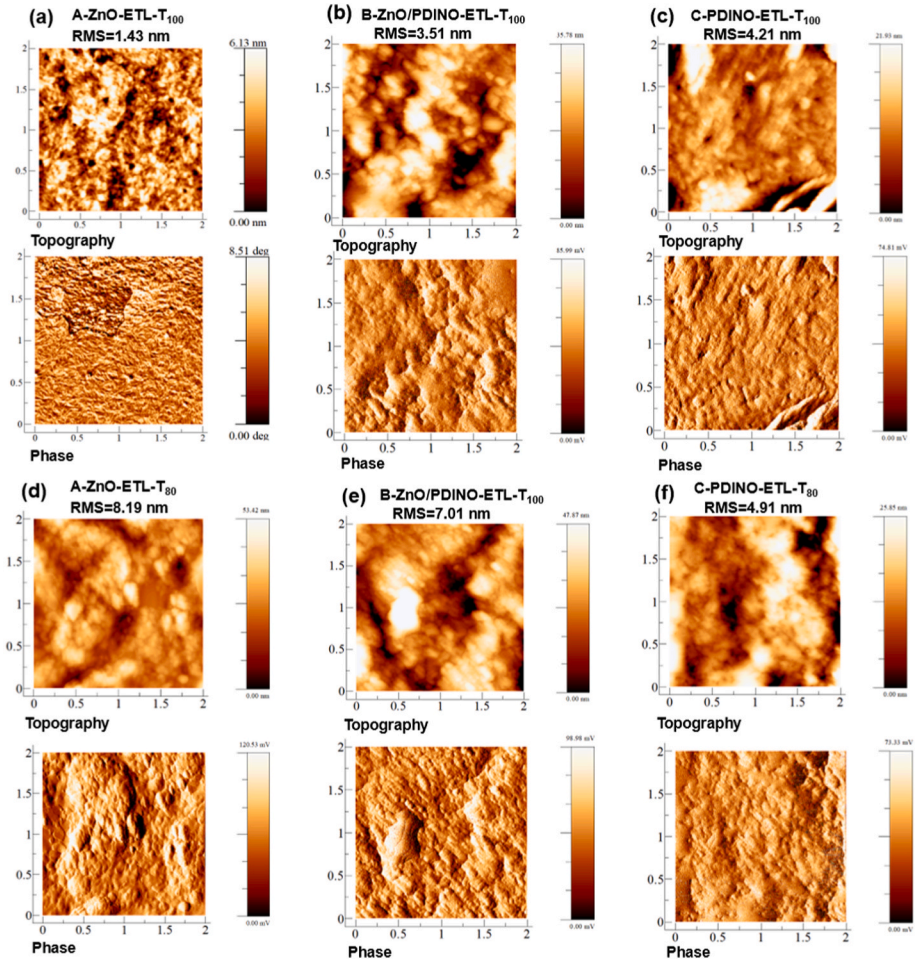

Fig. 9. AFM topography and phase images of the PM6:Y7 blend films over different ETLs of T_{100} (a) A-ZnO, (b) B–ZnO/PDINO, (c) C-PDINO based films and the T_{80} photo-degraded (d) A-ZnO, (e) B–ZnO/PDINO, (f) C-PDINO based films.

the photo-active blend and showing better resistance toward the illumination.

Atomic force microscope (AFM) characteristics were performed to investigate the active blend morphology changes during the photo-aging test. AFM images and the corresponding phases were demonstrated in Fig. 9 for both T_{100} fresh and T_{80} photo-aged tested based films of ITO/ETLs/active blend, considering the T_{80} photo-aging times of the corresponding devices as listed in Table 2. Regarding the T_{100} fresh films, we can clearly see that the A-ZnO based films (ITO/ZnO/PM6:Y7 film) showed the lowest root mean square (RMS) value of 1.43 nm (Fig. 9a), representing lowest surface roughness. Moreover, B–ZnO/PDIBO (ITO/ZnO/PDINO/PM6:Y7) and C-PDINO (ITO/PDINO/PM6:Y7) based films exhibited higher RMS values of 3.51 and 4.21 nm, respectively (Fig. 9b and c). This behavior agreed with the lowest R_S along with the highest FF values obtained for the T_{100} A-ZnO based devices and the contrary behavior of the B and C based devices as obtained from the J-V characteristics (Table 1) due to their higher surface roughness. In addition, this observation might reveal the higher performance of the T_{100} fresh A-ZnO based devices than the others.

However, after the T_{80} photo-aging test, we found that a huge increase in the surface roughness with RMS value of 8.19 nm (7 times higher than T_{100}) was observed for the A-ZnO based exposed films (Fig. 9d), explaining the FF as well the PCE burn in photo-degradation behavior (Fig. 2) along with the highest leakage current (Fig. 3a) exhibited for the A-ZnO based devices within short time of 2.5 h. Interestingly, same behavior was observed from the reported work of L. Duan et al. [42]. In addition, more stable attitude was obtained by B–ZnO/PDINO based films, where the RMS values were doubled to 7.01 nm (Fig. 9e). Surprisingly, T_{80} C-PDINO based exposed film presented a quite similar RMS value of 4.91 as compared to the T_{100} fresh films even after prolonged photo-aging time of 520 min. In addition, it showed lower RMS value among the further T_{80} devices, conserving the suitable phase separation and better pathways in the active layer [73]. Hence, we observed a noticeable effect regarding the photo-aging response upon changing the ETL. First, with reference to the A-ZnO based films, during the photo-degradation, it is suspected that photocatalytic effect plays a significant role in transferring the degradation to the contacted active blend, appeared to induce a greater extent of the film surface roughness. Where, the high RMS value with rough surface morphology indicated significant aggregation existence inside the active blend, which correspond the large phase separated domains with more excitons traps that in turn affect the charge dissociation process [16,92,93]. This observation is highly matched with the obtained R_2 fitted value (Table S4) from the previously discussed IS measurements, which showed a great increase in its value after the T_{80} photo-aging test along with a noticeable enlargement in the arc diameter of the A-ZnO-based devices (Fig. 8a).

Second, with respect to the C-PDINO based films, we suggested that the PDINO layer resist the photo-degradation and in turn preserve the blend film from degradation that presented in maintaining the roughness of the films over the photo-aging time. This agreed with the consistency of the resistance fitted values, R_1 and R_2 of the C-PDINO based devices that characterized by the IS discussed in Fig. 8c, along with the J_{SC} and R_S values obtained by the J-V characteristic over photo-aging times (Fig. 2, Table 1) as well as the constant leakage current behavior (Fig. 3c). Finally, it was interesting to find that the B–ZnO/PDINO films as well as the B-based devices performance showed a moderate behavior between both A and C ones, reflecting the effect of adding the PDINO film in increasing the photostability of the blend and in turn the full devices. Upon this context, we noticed that the photostability of the fabricated i-OSCs enhanced through avoiding the interface contact between the active layer and the ZnO film along with providing a good compatibility with the PDINO host system.

4. Conclusion

In conclusion, we presented an extremely efficient PDINO based cathode interlayer for iNF-OSCs, achieving excellent photostability behavior. The iNF-OSCs incorporating the PDINO interlayer (C-PDINO based devices) maintained 80% of the initial efficiency after continuous illumination (AM 1.5G, 100 mW cm^{-2}) for 520 min, while the ZnO-based control iNF-OSCs (A-ZnO based devices) remained only for 160 min under same conditions. The remarkable photostability of the C-PDINO based devices were mainly attributed to the avoidance of the photo-induced shunts and the photocatalytic behavior, which are inevitably in the ZnO based i-OSCs. Moreover, C-PDINO based devices refrained from the burn-in photo-degradation phenomena, which cause a significant reduction in the performance of the exposed devices by providing negative effects on energy transfer, exciton dissociation and charge recombination processes which may be more related to the bulk of the active layer as appeared for the ZnO based iNF-OSCs. Hence, this piece of work clearly demonstrates that PDINO is a promising cathode interlayer for tremendously photostable i-OSCs, particularly for large-scale production. As it fits the requirements of low-temperature fabrication, can be used in very fine-tuned thicknesses, showing great resistance behavior toward light, and does not react with the contacted active layers and electrodes.

CRediT authorship contribution statement

Enas Moustafa: Conceptualization, Data curation, Formal analysis, Visualization, Writing – original draft, Investigation. **Maria Méndez:** Data curation, Formal analysis, Investigation. **Josep Pallarès:** Conceptualization, Formal analysis, Investigation, Methodology, Supervision, Validation, Writing – review & editing, Funding acquisition. **Lluis F. Marsal:** Conceptualization, Formal analysis, Funding acquisition, Investigation, Methodology, Project administration, Supervision, Validation, Writing – review & editing.

Declaration of competing interest

The authors declare that they have no known competing financial interests or personal relationships that could have appeared to influence the work reported in this paper.

Data availability

Data will be made available on request.

Acknowledgements

Enas Moustafa acknowledges the Agency for Management of University and Research Grants (AGAUR) for receiving the fund with grant number 2019 FI_B01102. This work was further supported by the Spanish Ministerio de Ciencia e Innovación, PDI2021-128342OB-I00, by the Catalan Institution for Research and Advanced Studies (ICREA) under the ICREA Academia Award 2021 and by AGAUR ref. 2017-SGR-1527. We further acknowledge the Diputació de Tarragona 2022–23. Finally, we would thank Prof. Emilio Palomares, Institute of Chemical Research of Catalonia-The Barcelona Institute of Science and Technology (ICIQ-BIST) and Catalan Institution for Research and Advanced Studies (ICREA), for his assistance.

Appendix A. Supplementary data

Supplementary data to this article can be found online at https://doi.org/10.1016/j.solmat.2022.111985.

References

[1] Y. Firdaus, V.M. Le Corre, J.I. Khan, Z. Kan, F. Laquai, P.M. Beaujuge, T. D. Anthopoulos, Key parameters requirements for non-fullerene-based organic solar cells with power conversion efficiency >20%, Adv. Sci. 6 (2019), 1802028.

[2] Y. Cui, H. Yao, J. Zhang, K. Xian, T. Zhang, L. Hong, Y. Wang, Y. Xu, K. Ma, C. An, C. He, Z. Wei, F. Gao, J. Hou, Single-Junction organic photovoltaic cells with approaching 18% efficiency, Adv. Mater. 32 (2020) 1–7.

[3] J. Lv, H. Tang, J. Huang, C. Yan, K. Liu, Q. Yang, D. Hu, R. Singh, J. Lee, S. Lu, G. Li, Z. Kan, Additive-induced miscibility regulation and hierarchical morphology enable 17.5% binary organic solar cells, Energy Environ. Sci. 14 (2021) 3044–3052.

[4] B. Kan, J. Zhang, F. Liu, X. Wan, C. Li, X. Ke, Y. Wang, H. Feng, Y. Zhang, G. Long, R.H. Friend, A.A. Bakulin, Y. Chen, Fine-tuning the energy levels of a nonfullerene small-molecule acceptor to achieve a high short-circuit current and a power conversion efficiency over 12% in organic solar cells, Adv. Mater. 30 (2018) 1–8.

[5] M.B. Upama, M.A. Mahmud, G. Conibeer, A. Uddin, Trendsetters in high-efficiency organic solar cells: toward 20% power conversion efficiency, Solar RRL 4 (2020) 1–16.

[6] L. Duan, N.K. Elumalai, Y. Zhang, A. Uddin, Progress in non-fullerene acceptor based organic solar cells, Sol. Energy Mater. Sol. Cell. 193 (2019) 22–65.

[7] H. Yao, J. Wang, Y. Xu, S. Zhang, J. Hou, Recent progress in chlorinated organic photovoltaic materials, Accounts Chem. Res. 53 (2020) 822.

[8] Q. Liu, Y. Jiang, K. Jin, J. Qin, J. Xu, W. Li, J. Xiong, J. Liu, Z. Xiao, K. Sun, S. Yang, X. Zhang, L. Ding, 18% Efficiency organic solar cells, Sci. Bull. 65 (2020) 272–275.

[9] H. Fu, Z. Wang, Y. Sun, Advances in non-fullerene acceptor based ternary organic solar cells, Solar RRL 2 (2018) 1–18.

[10] P. Xue, S. Dai, T.K. Lau, J. Yu, J. Zhou, Y. Xiao, K. Meng, Z. Xie, G. Lu, X. Lu, R.P. S. Han, X. Zhan, High-performance nonfullerene organic solar cells with unusual inverted structure, Solar RRL 4 (2020) 1–8.

[11] T. Zhu, L. Zheng, Z. Xiao, X. Meng, L. Liu, L. Ding, X. Gong, Functionality of non-fullerene electron acceptors in ternary organic solar cells, Solar RRL 3 (2019) 1–8.

[12] N. Tokmoldin, S.M. Hosseini, M. Raoufi, L.Q. Phuong, O.J. Sandberg, H. Guan, Y. Zou, D. Neher, S. Shoaee, Extraordinarily long diffusion length in PM6:Y6 organic solar cells, J. Mater. Chem. 8 (2020) 7854–7860.

[13] J. Yuan, Y. Zhang, L. Zhou, G. Zhang, H.L. Yip, T.K. Lau, X. Lu, C. Zhu, H. Peng, P. A. Johnson, M. Leclerc, Y. Cao, J. Ulanski, Y. Li, Y. Zou, Single-Junction organic solar cell with over 15% efficiency using fused-ring acceptor with electron-deficient core, Joule 3 (2019) 1140–1151.

[14] J. Gao, Y. Li, S. Li, X. Xia, X. Lu, M. Shi, H. Chen, Non-fullerene acceptors with nitrogen-containing six-membered heterocycle cores for the applications in organic solar cells, Sol. Energy Mater. Sol. Cell. 225 (2021), 111046.

[15] M. Cui, D. Li, X. Du, N. Li, Q. Rong, N. Li, L. Shui, G. Zhou, X. Wang, C.J. Brabec, L. Nian, A cost-effective, aqueous-solution-processed cathode interlayer based on organosilica nanodots for highly efficient and stable organic solar cells, Adv. Mater. 32 (2020) 1–8.

[16] L. Duan, H. Yi, Y. Zhang, F. Haque, C. Xu, A. Uddin, Comparative study of light- and thermal-induced degradation for both fullerene and non-fullerene-based organic solar cells, Sustain. Energy Fuels 3 (2019) 723–735.

[17] S. Holliday, R.S. Ashraf, A. Wadsworth, D. Baran, S.A. Yousaf, C.B. Nielsen, C. H. Tan, S.D. Dimitrov, Z. Shang, N. Gasparini, M. Alamoudi, F. Laquai, C.J. Brabec, A. Salleo, J.R. Durrant, I. McCulloch, High-efficiency and air-stable P3HT-based polymer solar cells with a new non-fullerene acceptor, Nat. Commun. 7 (2016) 1–11.

[18] L. Hu, Y. Jiang, L. Sun, C. Xie, F. Qin, W. Wang, Y. Zhou, Significant enhancement of illumination stability of nonfullerene organic solar cells via an aqueous polyethylenimine modification, J. Phys. Chem. Lett. 12 (2021) 2607–2614.

[19] M. Günther, D. Blätte, A.L. Oechsle, S.S. Rivas, A.A. Yousefi Amin, P. Müller-Buschbaum, T. Bein, T. Ameri, Increasing photostability of inverted nonfullerene organic solar cells by using fullerene derivative additives, ACS Appl. Mater. Interfaces 13 (2021) 19072–19084.

[20] X. Du, T. Heumueller, W. Gruber, O. Almora, A. Classen, J. Qu, F. He, T. Unruh, N. Li, C.J. Brabec, Unraveling the microstructure-related device stability for polymer solar cells based on nonfullerene small-molecular acceptors, Adv. Mater. 32 (2020), 1908305.

[21] W. Yang, Z. Luo, R. Sun, J. Guo, T. Wang, Y. Wu, W. Wang, J. Guo, Q. Wu, M. Shi, H. Li, C. Yang, J. Min, acceptor additive, Nat. Commun. 11 (2020) 1–10.

[22] Y. Li, Y. Lin, Planar heterojunctions for reduced non-radiative open-circuit voltage loss and enhanced stability of organic solar cells, Mater. Chem. C 9 (2021) 11715–11721.

[23] S. Li, L. Zhan, F. Liu, J. Ren, M. Shi, C.Z. Li, T.P. Russell, H. Chen, An unfused-core-based nonfullerene acceptor enables high-efficiency organic solar cells with excellent morphological stability at high temperatures, Adv. Mater. 30 (2018), 1705208.

[24] J. Xiao, M. Ren, G. Zhang, J. Wang, D. Zhang, L. Liu, N. Li, C.J. Brabec, H. Yip, Y. Cao, An operando study on the photostability of nonfullerene organic solar cells, Solar RRL 3 (2019), 1900077.

[25] S. Huang, B. Kang, L. Duan, D. Zhang, Highly efficient inverted polymer solar cells by using solution processed MgO/ZnO composite interfacial layers, J. Colloid Interface Sci. 583 (2021) 178–187.

[26] M.T. Lloyd, D.C. Olson, P. Lu, E. Fang, D.L. Moore, M.S. White, M.O. Reese, D. S. Ginley, J.W.P. Hsu, Impact of contact evolution on the shelf life of organic solar cells, J. Mater. Chem. 19 (2009) 7638–7642.

[27] B.A. Macleod, B.J. Tremolet De Villers, P. Schulz, P.F. Ndione, H. Kim, A. J. Giordano, K. Zhu, S.R. Marder, S. Graham, J.J. Berry, A. Kahn, D.C. Olson, Stability of inverted organic solar cells with ZnO contact layers deposited from precursor solutions, Energy Environ. Sci. 8 (2015) 592–601.

[28] L.K. Jagadamma, M. Abdelsamie, A. El Labban, E. Aresu, G.O. Ngongang Ndjawa, D.H. Anjum, D. Cha, P.M. Beaujuge, A. Amassian, Efficient inverted bulk-heterojunction solar cells from low-temperature processing of amorphous ZnO buffer layers, J. Mater. Chem. 2 (2014) 13321–13331.

[29] V.S. Balderrama, J.G. Sánchez, G. Lastra, W. Cambarau, S. Arias, J. Pallarès, E. Palomares, M. Estrada, L.F. Marsal, High-efficiency organic solar cells based on a halide salt and polyfluorene polymer with a high alignment-level of the cathode selective contact, J. Mater. Chem. 6 (2018) 22534–22544.

[30] H. Naz, R.N. Ali, Q. Liu, S. Yang, B. Xiang, Niobium doped zinc oxide nanorods as an electron transport layer for high-performance inverted polymer solar cells, J. Colloid Interface Sci. 512 (2018) 548–554.

[31] J.C. Ke, Y.H. Wang, K.L. Chen, C.J. Huang, Effect of organic solar cells using various power O2 plasma treatments on the indium tin oxide substrate, J. Colloid Interface Sci. 465 (2016) 311–315.

[32] M.A. Ibrahem, H.Y. Wei, M.H. Tsai, K.C. Ho, J.J. Shyue, C.W. Chu, Solution-processed zinc oxide nanoparticles as interlayer materials for inverted organic solar cells, Sol. Energy Mater. Sol. Cell. 108 (2013) 156–163.

[33] C.B. Ong, L.Y. Ng, A.W. Mohammad, A review of ZnO nanoparticles as solar photocatalysts: synthesis, mechanisms and applications, Renew. Sustain. Energy Rev. 81 (2018) 536–551.

[34] A. Manor, E.A. Katz, T. Tromholt, F.C. Krebs, T. Tromholt, F.C. Krebs, Electrical and photo-induced degradation of ZnO layers in organic photovoltaics, Adv. Energy Mater. 1 (2011) 836–843.

[35] E. Moustafa, J.G. Sánchez, L.F. Marsal, J. Pallarès, Stability enhancement of high-performance inverted polymer solar cells using ZnO electron interfacial layer deposited by intermittent spray pyrolysis approach, ACS Appl. Energy Mater. 4 (2021) 4099–4111.

[36] A.A.A. Torimtubun, J.G. Sánchez, J. Pallarès, L.F. Marsal, A cathode interface engineering approach for the comprehensive study of indoor performance enhancement in organic photovoltaics, Sustain. Energy Fuels 4 (2020) 3378–3387.

[37] E. Moustafa, A.A.A. Torimtubun, J. Pallarès, L.F. Marsal, Effect of additives and annealing on the performance of nonfullerene-based binary and ternary organic photovoltaics, Solar RRL 2100480 (2021) 1–16.

[38] R.C.I. Mackenzie, V.S. Balderrama, S. Schmeisser, R. Stoof, S. Greedy, J. Pallarès, L. F. Marsal, A. Chanaewa, E. Von Hauff, Loss mechanisms in high efficiency polymer solar cells, Adv. Energy Mater. 6 (2016) 2–8.

[39] M.O. Reese, S.A. Gevorgyan, M. Jørgensen, E. Bundgaard, S.R. Kurtz, D.S. Ginley, D.C. Olson, M.T. Lloyd, P. Morvillo, E.A. Katz, A. Elschner, O. Haillant, T. R. Currier, V. Shrotriya, M. Hermenau, M. Riede, K.R. Kirov, G. Trimmel, T. Rath, O. Inganäs, F. Zhang, M. Andersson, K. Tvingstedt, M. Lira-Cantu, D. Laird, C. McGuiness, S. Gowrisanker, M. Pannone, M. Xiao, J. Hauch, R. Steim, D. M. Delongchamp, R. Rösch, H. Hoppe, N. Espinosa, A. Urbina, G. Yaman-Uzunoglu, J.B. Bonekamp, A.J.J.M. Van Breemen, C. Girotto, E. Voroshazi, F.C. Krebs, Consensus stability testing protocols for organic photovoltaic materials and devices, Sol. Energy Mater. Sol. Cell. 95 (2011) 1253–1267.

[40] N. Gasparini, M. Salvador, S. Strohm, T. Heumueller, I. Levchuk, A. Wadsworth, J. H. Bannock, J.C. de Mello, H.J. Egelhaaf, D. Baran, I. McCulloch, C.J. Brabec, Burn-in free nonfullerene-based organic solar cells, Adv. Energy Mater. 7 (2017) 1–7.

[41] X. Zhang, J. Cai, C. Guo, D. Li, B. Du, Y. Zhuang, S. Cheng, L. Wang, D. Liu, T. Wang, Simultaneously enhanced efficiency and operational stability of nonfullerene organic solar cells via solid-additive-mediated aggregation control, Small 17 (2021) 1–10.

[42] L. Duan, X. Meng, Y. Zhang, H. Yi, K. Jin, F. Haque, C. Xu, Z. Xiao, L. Ding, A. Uddin, Comparative analysis of burn-in photo-degradation in non-fullerene COi8DFIC acceptor based high-efficiency ternary organic solar cells, Mater. Chem. Front. 3 (2019) 1085–1096.

[43] R. Roesch, T. Faber, E. Von Hauff, T.M. Brown, M. Lira-Cantu, H. Hoppe, Procedures and practices for evaluating thin-film solar cell stability, Adv. Energy Mater. 5 (2015) 1–24.

[44] W.R. Mateker, M.D. McGehee, Progress in understanding degradation mechanisms and improving stability in organic photovoltaics, Adv. Mater. 29 (2017), 1603940.

[45] N. Gasparini, S.H.K. Paleti, J. Bertrandie, G. Cai, G. Zhang, A. Wadsworth, X. Lu, H.-L. Yip, I. McCulloch, D. Baran, Exploiting ternary blends for improved photostability in high-efficiency organic solar cells, ACS Energy Lett. 5 (2020) 1371–1379.

[46] Y. Jiang, L. Sun, F. Jiang, C. Xie, L. Hu, X. Dong, F. Qin, T. Liu, L. Hu, X. Jiang, Y. Zhou, Photocatalytic effect of ZnO on the stability of nonfullerene acceptors and its mitigation by SnO2 for nonfullerene organic solar cells, Mater. Horiz. 6 (2019) 1438–1443.

[47] W. Xu, R. Xia, T. Ye, L. Zhao, Z. Kan, Y. Mei, C. Yan, X.W. Zhang, W.Y. Lai, P. E. Keivanidis, W. Huang, Understanding the light soaking effects in inverted organic solar cells functionalized with conjugated macroelectrolyte electron-collecting interlayers, Adv. Sci. 3 (2015) 1–7.

[48] T. Kusumi, T. Kuwabara, K. Fujimori, T. Minami, T. Yamaguchi, T. Taima, K. Takahashi, T. Murakami, V.A.S.A. Rachmat, K. Marumoto, Mechanism of light-soaking effect in inverted polymer solar cells with open-circuit voltage increase, ACS Omega 2 (2017) 1617–1624.

[49] S. Trost, K. Zilberberg, A. Behrendt, A. Polywka, P. Görrn, P. Reckers, J. Maibach, T. Mayer, T. Riedl, Overcoming the "light-soaking" issue in inverted organic solar cells by the use of al:zno electron extraction layers, Adv. Energy Mater. 3 (2013) 1437–1444.

[50] B. Ecker, H.J. Egelhaaf, R. Steim, J. Parisi, E. Von Hauff, Understanding S-shaped current-voltage characteristics in organic solar cells containing a TiO x interlayer with impedance spectroscopy and equivalent circuit analysis, J. Phys. Chem. C 116 (2012) 16333–16337.

[51] A. Sundqvist, O.J. Sandberg, M. Nyman, J.H. Smått, R. Österbacka, Origin of the S-shaped JV curve and the light-soaking issue in inverted organic solar cells, Adv. Energy Mater. 6 (2016) 1–7.

[52] M. Dusza, W. Strek, F. Granek, Significance of light-soaking effect in proper analysis of degradation dynamics of organic solar cells, J. Photon. Energy 6 (2016), 035503.
[53] F.J. Lim, Y.T. Set, A. Krishnamoorthy, J. Ouyang, J. Luther, G.W. Ho, Addressing the light-soaking issue in inverted organic solar cells using chemical bath deposited fluorinated TiOx electron transport layer, J. Mater. Chem. 3 (2015) 314–322.
[54] T. Kuwabara, K. Yano, T. Yamaguchi, T. Taima, K. Takahashi, D. Son, K. Marumoto, Mechanistic investigation into the light soaking effect observed in inverted polymer solar cells containing chemical bath deposited titanium oxide, J. Phys. Chem. C 119 (2015) 5274–5280.
[55] I.I. Jeon, Y. Matsuo, Vertical phase separation and light-soaking effect improvements by photoactive layer spin coating initiation time control in air-processed inverted organic solar cells, Sol. Energy Mater. Sol. Cell. 140 (2015) 335–343.
[56] P. Schilinsky, C. Waldauf, J. Hauch, C.J. Brabec, Simulation of light intensity dependent current characteristics of polymer solar cells, J. Appl. Phys. 95 (2004) 2816–2819.
[57] N. Grossiord, J.M. Kroon, R. Andriessen, P.W.M. Blom, Degradation mechanisms in organic photovoltaic devices, Org. Electron. 13 (2012) 432–456.
[58] S.L.M. Van Mensfoort, R. Coehoorn, Determination of injection barriers in organic semiconductor devices from capacitance measurements, Phys. Rev. Lett. 100 (2008) 1–4.
[59] S.R. Cowan, R.A. Street, S. Cho, A.J. Heeger, Transient photoconductivity in polymer bulk heterojunction solar cells: competition between sweep-out and recombination, Phys. Rev. B Condens. Matter 83 (2011) 1–8.
[60] S.R. Cowan, A. Roy, A.J. Heeger, Recombination in polymer-fullerene bulk heterojunction solar cells, Phys. Rev. B Condens. Matter 82 (2010) 10.
[61] V.V. Brus, Light dependent open-circuit voltage of organic bulk heterojunction solar cells in the presence of surface recombination, Org. Electron. 29 (2016) 1–6.
[62] C.M. Proctor, T.Q. Nguyen, Effect of leakage current and shunt resistance on the light intensity dependence of organic solar cells, Appl. Phys. Lett. 106 (2015), 083301.
[63] G. Juka, K. Arlauskas, Charge carrier recombination in bulk heterojunction organic solar cells, Sol. Energy 38 (2010) 1941–1960.
[64] Z. Liu, N. Wang, Small energy loss in ternary organic solar cells with a blend of cascade energy levels: two fullerene-free acceptors as the electron acceptor, J. Mater. Chem. C 7 (2019) 10039–10048.
[65] J. Oh, S. Jung, M. Jeong, B. Lee, J. Lee, Y. Cho, S.M. Lee, S. Chen, Z.G. Zhang, Y. Li, C. Yang, Ring-perfluorinated non-volatile additives with a high dielectric constant lead to highly efficient and stable organic solar cells, J. Mater. Chem. C 7 (2019) 4716–4724.
[66] M. Lenes, M. Morana, C.J. Brabec, P.W.M. Blom, Recombination-limited photocurrents in low bandgap polymer/fullerene solar cells, Adv. Funct. Mater. 19 (2009) 1106–1111.
[67] V. Gupta, A.K.K. Kyaw, D.H. Wang, S. Chand, G.C. Bazan, A.J. Heeger, Barium: An efficient cathode layer for bulk-heterojunction solar cells, Sci. Rep. 3 (2013) 6–11.
[68] P. Hartnagel, T. Kirchartz, Understanding the light-intensity dependence of the short-circuit current of organic solar cells, Adv. Theory Simulat. 3 (2020) 1–11.
[69] J.-L. Wu, F.-C. Chen, Y.-S. Hsiao, F.-C. Chien, P. Chen, C.-H. Kuo, M.H. Huang, C.-S. Hsu, Nanoparticles on the performance of polymer bulk heterojunction solar cells, ACS Nano 5 (2011) 959–967.
[70] B.H. Jiang, Y.P. Wang, C.Y. Liao, Y.M. Chang, Y.W. Su, R.J. Jeng, C.P. Chen, Improved blend film morphology and free carrier generation provide a high-performance ternary polymer solar cell, ACS Appl. Mater. Interfaces 13 (2021) 1076–1085.
[71] V.D. Mihailetchi, L.J.A. Koster, P.W.M. Blom, C. Melzer, B. De Boer, J.K.J. Van Duren, R.A.J. Janssen, Compositional dependence of the performance of poly(p-phenylene vinylene):Methanofullerene bulk-heterojunction solar cells, Adv. Funct. Mater. 15 (2005) 795–801.
[72] V.D. Mihailetchi, L.J.A. Koster, J.C. Hummelen, P.W.M. Blom, Photocurrent generation in polymer-fullerene bulk heterojunctions, Phys. Rev. Lett. 93 (2004) 19–22.
[73] X. Kong, H. Lin, X. Du, L. Li, X. Li, X. Chen, C. Zheng, D. Wang, S. Tao, Hydrogen bond induced high performance ternary fullerene-free organic solar cells with increased current density and enhanced stability, J. Mater. Chem. C 6 (2018) 9691–9702.
[74] S. Liu, J. Yuan, W. Deng, M. Luo, Y. Xie, Q. Liang, Y. Zou, Z. He, H. Wu, Y. Cao, High-efficiency organic solar cells with low non-radiative recombination loss and low energetic disorder, Nat. Photonics 14 (2020) 300–305.
[75] N. Jain, N. Chandrasekaran, A. Sadhanala, R.H. Friend, C.R. McNeill, D. Kabra, Interfacial disorder in efficient polymer solar cells: the impact of donor molecular structure and solvent additives, J. Mater. Chem. 5 (2017) 24749–24757.
[76] Z. He, B. Xiao, F. Liu, H. Wu, Y. Yang, S. Xiao, C. Wang, T.P. Russell, Y. Cao, Single-junction polymer solar cells with high efficiency and photovoltage, Nat. Photonics 9 (2015) 174–179.
[77] F. Urbach, The long-wavelength edge of photographic sensitivity and of the electronic Absorption of Solids [8], Phys. Rev. 92 (1953) 1324.
[78] C.H. Peters, I.T. Sachs-Quintana, W.R. Mateker, T. Heumueller, J. Rivnay, R. Noriega, Z.M. Beiley, E.T. Hoke, A. Salleo, M.D. McGehee, The mechanism of burn-in loss in a high efficiency polymer solar cell, Adv. Mater. 24 (2012) 663–668.
[79] S.A. Hawks, F. Deledalle, J. Yao, D.G. Rebois, G. Li, J. Nelson, Y. Yang, T. Kirchartz, J.R. Durrant, Relating recombination, density of states, and device performance in an effi cient polymer:fullerene organic solar cell blend, Adv. Energy Mater. 3 (2013) 1201–1209.
[80] E. Von Hauff, Impedance spectroscopy for emerging photovoltaics, J. Phys. Chem. C 123 (2019) 11329–11346.
[81] G. Garcia-Belmonte, A. Munar, E.M. Barea, J. Bisquert, I. Ugarte, R. Pacios, Charge carrier mobility and lifetime of organic bulk heterojunctions analyzed by impedance spectroscopy, Org. Electron. 9 (2008) 847–851.
[82] B. Ecker, J.C. Nolasco, J. Pallarés, L.F. Marsal, J. Posdorfer, J. Parisi, E. Von Hauff, Degradation effects related to the hole transport layer in organic solar cells, Adv. Funct. Mater. 21 (2011) 2705–2711.
[83] H.F. Haneef, A.M. Zeidell, O.D. Jurchescu, Charge carrier traps in organic semiconductors: a review on the underlying physics and impact on electronic devices, J. Mater. Chem. C 8 (2020) 759–787.
[84] T. Walter, R. Herberholz, C. Müller, H.W. Schock, Determination of defect distributions from admittance measurements and application to Cu(In,Ga)Se2 based heterojunctions, J. Appl. Phys. 80 (1996) 4411–4420.
[85] J. Bhattacharya, P.H. Joshi, R. Biswas, V.L. Dalal, Pathway for recovery of photo-degraded polymer solar cells by post degradation thermal anneal, Sol. Energy Mater. Sol. Cell. 164 (2017) 70–79.
[86] J. Wu, J. Luke, H.K.H. Lee, P. Shakya Tuladhar, H. Cha, S.Y. Jang, W.C. Tsoi, M. Heeney, H. Kang, K. Lee, T. Kirchartz, J.S. Kim, J.R. Durrant, Tail state limited photocurrent collection of thick photoactive layers in organic solar cells, Nat. Commun. 10 (2019) 1–10.
[87] R.C.I. Mackenzie, C.G. Shuttle, G.F. Dibb, N. Treat, E. Von Hauff, M.J. Robb, C. J. Hawker, M.L. Chabinyc, J. Nelson, Interpreting the density of states extracted from organic solar cells using transient photocurrent measurements, J. Phys. Chem. C 117 (2013) 12407–12414.
[88] D. Credgington, J.R. Durrant, Insights from transient optoelectronic analyses on the open-circuit voltage of organic solar cells, J. Phys. Chem. Lett. 3 (2012) 1465–1478.
[89] E. Osorio, J.G. Sánchez, L.N. Acquaroli, M. Pacio, J. Ferré-Borrull, J. Pallarès, L. F. Marsal, Degradation analysis of encapsulated and nonencapsulated TiO2/PTB7: PC70BM/V2O5 solar cells under ambient conditions via impedance spectroscopy, ACS Omega 2 (2017) 3091–3097.
[90] Z. He, K. Huang, C. Guo, Z. Jin, C. Hou, A Debye dispersion model of a two-layered material, AIP Adv. 9 (2019), 045321.
[91] H. Schroeder, Poole-Frenkel-effect as dominating current mechanism in thin oxide films - an illusion? J. Appl. Phys. 117 (2015), 215103.
[92] J. Wan, X. Xu, G. Zhang, Y. Li, K. Feng, Q. Peng, Highly efficient halogen-free solvent processed small-molecule organic solar cells enabled by material design and device engineering, Energy Environ. Sci. 10 (2017) 1739–1745.
[93] Q. An, F. Zhang, L. Li, J. Wang, J. Zhang, L. Zhou, W. Tang, Improved efficiency of bulk heterojunction polymer solar cells by doping low-bandgap small molecules, ACS Appl. Mater. Interfaces 6 (2014) 6537–6544.